This is a repository copy of *TIC 378898110: A bright, short-period AM CVn binary in TESS*.

White Rose Research Online URL for this paper:
https://eprints.whiterose.ac.uk/205379/

Version: Published Version

Article:
Green, M.J. orcid.org/0000-0002-0948-4801, Hermes, J.J. orcid.org/0000-0001-5941-2286, Barlow, B.N. et al. (22 more authors) (2024) TIC 378898110: A bright, short-period AM CVn binary in TESS. Monthly Notices of the Royal Astronomical Society, 527 (2). pp. 3445-3458. ISSN 0035-8711

https://doi.org/10.1093/mnras/stad3412

Reuse
This article is distributed under the terms of the Creative Commons Attribution (CC BY) licence. This licence allows you to distribute, remix, tweak, and build upon the work, even commercially, as long as you credit the authors for the original work. More information and the full terms of the licence here: https://creativecommons.org/licenses/

Takedown
If you consider content in White Rose Research Online to be in breach of UK law, please notify us by emailing eprints@whiterose.ac.uk including the URL of the record and the reason for the withdrawal request.

eprints@whiterose.ac.uk
https://eprints.whiterose.ac.uk/

Monthly Notices of the ROYAL ASTRONOMICAL SOCIETY

MNRAS **527,** 3445–3458 (2024)
Advance Access publication 2023 November 3

https://doi.org/10.1093/mnras/stad3412

TIC 378898110: A bright, short-period AM CVn binary in *TESS*

Matthew J. Green [1,2,3★], J. J. Hermes [4], Brad N. Barlow,[5,6] T. R. Marsh [3], Ingrid Pelisoli [3], Boris T. Gänsicke [3], Ben C. Kaiser,[6] Alejandra Romero [7], Larissa Antunes Amaral,[7,8] Kyle Corcoran,[9] Dirk Grupe,[10] Mark R. Kennedy [11,12], S. O. Kepler [7], James Munday [3,13], R. P. Ashley,[3] Andrzej S. Baran,[14,15] Elmé Breedt [16], Alex J. Brown,[17] V. S. Dhillon [17,18], Martin J. Dyer [17], Paul Kerry,[17] George W. King [3,19], S. P. Littlefair,[17] Steven G. Parsons [17] and David I. Sahman[17]

Affiliations are listed at the end of the paper

Accepted 2023 November 2. Received 2023 November 2; in original form 2023 July 1

ABSTRACT

AM CVn-type systems are ultracompact, helium-accreting binary systems that are evolutionarily linked to the progenitors of thermonuclear supernovae and are expected to be strong Galactic sources of gravitational waves detectable to upcoming space-based interferometers. AM CVn binaries with orbital periods $\lesssim$20–23 min exist in a constant high state with a permanently ionized accretion disc. We present the discovery of TIC 378898110, a bright ($G = 14.3$ mag), nearby (309.3 ± 1.8 pc), high-state AM CVn binary discovered in *TESS* two-minute-cadence photometry. At optical wavelengths, this is the third-brightest AM CVn binary known. The photometry of the system shows a 23.07172(6) min periodicity, which is likely to be the 'superhump' period and implies an orbital period in the range 22–23 min. There is no detectable spectroscopic variability. The system underwent an unusual, year-long brightening event during which the dominant photometric period changed to a shorter period (constrained to 20.5 ± 2.0 min), which we suggest may be evidence for the onset of disc-edge eclipses. The estimated mass transfer rate, $\log(\dot{M}/\mathrm{M}_\odot\,\mathrm{yr}^{-1}) = -6.8 \pm 1.0$, is unusually high and may suggest a high-mass or thermally inflated donor. The binary is detected as an X-ray source, with a flux of $9.2^{+4.2}_{-1.8} \times 10^{-13}\,\mathrm{erg\,cm^{-2}\,s^{-1}}$ in the 0.3–10 keV range. TIC 378898110 is the shortest-period binary system discovered with *TESS*, and its large predicted gravitational-wave amplitude makes it a compelling verification binary for future space-based gravitational wave detectors.

Key words: binaries: close – stars: dwarf novae – stars: individual: TIC 378898110 – novae, cataclysmic variables – white dwarfs.

1 INTRODUCTION

AM CVn-type binary systems are ultracompact, mass-transferring binary systems with orbital periods in the range 5–68 min (e.g. Solheim 2010; Green et al. 2020). Each AM CVn binary consists of a white dwarf accreting helium-dominated matter from a degenerate or semi-degenerate donor star. Short-period AM CVn binary systems are expected to be among the first handful of individual Galactic sources of gravitational waves in the frequency range visible to space-based interferometers such as the Laser Interferometer Space Antenna (*LISA*; Kremer et al. 2017; Breivik et al. 2018; Kupfer et al. 2018, 2023). Their evolutionary channels are linked to double white dwarf binaries, a significant channel for Type Ia Supernovae (e.g. Bildsten et al. 2007; Kilic et al. 2014; Maoz, Mannucci & Nelemans 2014).

A variety of progenitor channels have been proposed for AM CVn binaries, in which the system may descend from a double white dwarf binary (Paczyński 1967; Deloye et al. 2007; Wong & Bildsten 2021), a binary consisting of a white dwarf and a compact helium-burning star (Savonije, de Kool & van den Heuvel 1986; Iben & Tutukov 1987; Yungelson 2008), or a cataclysmic variable with an evolved donor (Podsiadlowski, Han & Rappaport 2003; Goliasch & Nelson 2015; Belloni & Schreiber 2023). The relative importance of these various channels remains an unsolved problem.

AM CVn binaries remain a rare class of object, with 56 known systems at the time of the last population review (Ramsay et al. 2018). Recent discoveries by Burdge et al. (2020b), van Roestel et al. (2021, 2022), Rivera Sandoval et al. (2021), and others, have increased the number of published systems to approximately 80, but many newly discovered systems are not suitable for in-depth characterization studies (for instance, using phase-resolved spectroscopy) due to their faintness.

The small sample size of known AM CVn binaries limits attempts to understand the population empirically, such as studies of the population density (Carter et al. 2013) or investigations into the question of how these systems form (Goliasch & Nelson 2015; Green et al. 2018; Ramsay et al. 2018; Wong & Bildsten 2021; Belloni & Schreiber 2023). Based on the *Gaia* parallaxes of the known systems, the sample of known AM CVn binaries may be incomplete even at distances of a few hundred parsecs (Ramsay et al. 2018).

★ E-mail: mjgreenastro@gmail.com

© The Author(s) 2023.
Published by Oxford University Press on behalf of Royal Astronomical Society. This is an Open Access article distributed under the terms of the Creative Commons Attribution License (http://creativecommons.org/licenses/by/4.0/), which permits unrestricted reuse, distribution, and reproduction in any medium, provided the original work is properly cited.

Downloaded from https://academic.oup.com/mnras/article/527/2/3445/7342474 by guest on 01 December 2023

Table 1. Summary of basic observational properties of TIC 378898110. The UVOT magnitude is given in the AB system, while others are given in the Vega magnitude system (as is customary). Sources for these magnitudes are given in Section 3.3.

Property	Value
TIC ID	378898110
Gaia ID	6058834949182961536
ICRS coords. (J2000)	12:03:38.7 − 60:22:48.0
Galactic coords.	297.055664 + 1.945349
Magnitudes:	
UVOT *UVW2*	14.41 ± 0.03
Gaia BP	14.271 ± 0.006
Gaia G	14.276 ± 0.003
Gaia RP	14.243 ± 0.006
2MASS J	14.11 ± 0.04
2MASS H	14.08 ± 0.05
2MASS K_s	14.11 ± 0.07
WISE W1	14.20 ± 0.06
WISE W2	14.40 ± 0.08

AM CVn accretion discs show a range of types of photometric behaviour, commonly explained by the disc instability model that also describes hydrogen-accreting cataclysmic variables (e.g. Tsugawa & Osaki 1997; Cannizzo & Nelemans 2015). This behaviour is driven by the mass transfer rate, $\dot{M}$, which correlates steeply with orbital period, $P_{\rm orb}$, as $\dot{M} \propto {P_{\rm orb}}^{-5.2}$ (Warner 1995; Tsugawa & Osaki 1997). If the population includes donor stars with differing levels of degeneracy (Deloye et al. 2007; Wong & Bildsten 2021), then some amount of scatter can be expected in the relationship between $P_{\rm orb}$ and $\dot{M}$, but the correlation should remain strong.

As a result, AM CVn binaries can be separated into several groups based on their accretion disc behaviour, which naturally sorts them as a function of orbital period (e.g. Solheim 2010). Short-period systems (7–12 $\lesssim P_{\rm orb} \lesssim$ 20–28 min) typically exist in a permanently ionized 'high' state, comparable to nova-like cataclysmic variables. Meanwhile, systems at somewhat longer periods (20–28 $\lesssim P_{\rm orb} \lesssim$ 45–58 min) spend the majority of their time in a neutral, quiescent state, with occasional dwarf nova outbursts. While most AM CVn binaries with $P_{\rm orb} >$ 20 min are outbursting or quiescent systems, two high-state systems have claimed orbital periods of 23 and 28 min (CXOGBS J1751-2940 and ZTF J2228+4949, though note that neither orbital period has been confirmed spectroscopically; Wevers et al. 2016; Burdge et al. 2020a).

High-state AM CVn binaries and AM CVn binaries in outburst can show a variety of photometric signatures. Assuming there are no eclipses, the strongest signal is typically a 'superhump' signal, which is driven by an interaction between the donor star and the accretion disc, and has a period within a few per cent of the orbital period (Patterson, Halpern & Shambrook 1993). The orbital period itself and the precession period of the accretion disc may be seen (e.g. Armstrong, Patterson & Kemp 2012; Green et al. 2018; Solanki et al. 2021), and some systems also show a variety of periodic signals with no conclusive physical interpretation (e.g. Fontaine et al. 2011; Kupfer et al. 2015).

In this work, we present the discovery of the high-state AM CVn binary TIC 378898110, which has properties presented in Table 1. The system was first identified as a short-period variable by its *TESS* photometry (*Transiting Exoplanet Survey Satellite*; Ricker et al. 2014). Follow-up observations from the ground led to its AM CVn classification. Its magnitude of $G = 14.3$ makes it the third-brightest AM CVn binary known by apparent magnitude, after HP Lib ($G = 13.6$) and the namesake of the class, AM CVn itself ($G = 14.0$). Its parallax from *Gaia* EDR3 (Gaia Collaboration et al. 2021) implies a distance of 306.2 ± 1.7 pc (Bailer-Jones et al. 2021), making it the 12th closest AM CVn binary. The likely orbital period of TIC 378898110 is ≈22–23 min, placing it in the overlap period range between high-state and outbursting systems.

In Section 2, we describe the observations undertaken for this work. Section 3 presents the photometric data obtained and its analysis, while Section 4 presents the spectroscopic data. Sections 5 and 6 discuss and summarize our findings regarding TIC 378898110.

2 OBSERVATIONS

A number of observations of TIC 378898110 were obtained and analysed for this work. These observations are summarized in Table 2.

2.1 *TESS* photometry

TIC 378898110 was observed by *TESS* with a two-minute cadence in Sectors 37 and 38, spanning a total coverage of 52 days. The target was proposed for two-minute cadence data under proposals G03124 (as a candidate low-mass white dwarf) and G03221 (as a candidate hot subdwarf, due to its inclusion in the hot subdwarf catalogue of Geier et al. 2019). These data were reduced by the Science Processing Operations Centre (SPOC).

The target is located in a crowded region of the sky, with an estimated *TESS* contamination factor (`CROWDSAP`) of 0.12; the relative amplitudes from SPOC light curves have been corrected to account for this flux dilution. A pixel-level analysis (Higgins & Bell 2023) showed that the periodic variability was likely to originate from TIC 378898110 itself, as was later confirmed by ground-based photometry.

A previous *TESS* observation in Sectors 10 and 11 (2019 March to May) had only a cadence of half an hour and was not able to fully resolve the dominant periodic signal.

2.2 Ground-based photometry

Follow-up photometry was obtained with the Goodman High Throughput Spectrograph (Clemens, Crain & Anderson 2004) on the 4.1-m Southern Astrophysical Research (SOAR) telescope at Cerro Pachón in Chile. These data were obtained using a broad, blue *S8612* filter. We obtained 443 exposures of 10 s, taken in the 200 Hz `ATTN2` readout mode with 2 × 2 binning and a reduced window on the chip to minimize readout overheads. The data were debiassed and flat-field corrected with standard IRAF routines, and aperture photometry was performed with DAOPHOT.

Further ground-based photometry was obtained using ULTRACAM, a high-speed, triple-beam photometer (Dhillon et al. 2007). For these observations, ULTRACAM was mounted on the 3.5-m New Technology Telescope (NTT) at La Silla observatory in Chile. The u_s, g_s, and i_s filters were used; these filters are designed to cover the same wavelengths as the Sloan $u'g'i'$ filters but with higher throughput (Dhillon et al. 2021). The wavelength coverage of these filters can be broken down into 3000–4000 Å for u_s, 3900–5700 Å for g_s, and 6700–8700 Å for i_s. Observations were obtained in 2021, 2022, and 2023.

The ULTRACAM data were reduced using the HiPERCAM pipeline (Dhillon et al. 2021). Each image was bias-subtracted and divided throughout by a flat-field image in the same filter that was obtained at twilight on the same night. No dark-frame subtraction

Downloaded from https://academic.oup.com/mnras/article/527/2/3445/7342474 by guest on 01 December 2023

Table 2. Summary of the observations presented in this work. For ULTRACAM observations, exposure times in brackets are those used for the u_s-band, which are increased to account for the lower throughput of that filter. Approximate wavelength coverages of photometric bandpasses are given, to aid the reader in comparison between different bands.

Instrument	Date	Filters / Wavelength [Å]	Exposure [s]	Total exposure [s]
Space-based phot.				
TESS	2021 Apr 02–May 26	*T* / 6000–10 000	120	4138200
Swift	2021 July 27	*UVW2* / 1600–3500	–	1240
Ground-based phot.				
Goodman + SOAR	2021 July 4	*S8612* / 3000–8400	10	7660
ULTRACAM + NTT	2021 July 14	$u_s g_s i_s$ / 3000–8700	2.8 (8.4)	6300
ULTRACAM + NTT	2022 March 05	$u_s g_s i_s$ / 3000–8700	3.5 (10.5)	3570
ULTRACAM + NTT	2022 March 06	$u_s g_s i_s$ / 3000–8700	3.0 (9.0)	4080
ULTRACAM + NTT	2022 March 28	$u_s g_s i_s$ / 3000–8700	3.0 (9.0)	4580
ULTRACAM + NTT	2023 March 08	$u_s g_s i_s$ / 3000–8700	3.0 (6.0)	9790
ULTRACAM + NTT	2023 March 09	$u_s g_s i_s$ / 3000–8700	3.0 (6.0)	2230
ULTRACAM + NTT	2023 March 10	$u_s g_s i_s$ / 3000–8700	3.0 (6.0)	4020
Spectroscopy				
Goodman + SOAR	2021 July 05	3600–5200	60	2940

was performed, but care was taken to avoid known hot pixels during target acquisition. The target flux was extracted using a variable aperture with width scaled to 1.7× the full-width half-maximum of the point-spread function in that image. The target flux was divided by a constant comparison star observed in the same image (coordinates 12:03:35.19−60:23:06.9, $G = 14.1$ mag) to correct for changes in atmospheric transparency.

2.3 *Swift* X-ray observations

Motivated by the presence of a *ROSAT* source within 15 arcsec of the target (1RXS J120340.6−602252),[1] X-ray observations were undertaken with the NASA Neil Gehrels Gamma-Ray Burst Exploer Mission *Swift* satellite (Gehrels et al. 2004) through its Target of Opportunity program (ToO ID 16045). The target was observed by *Swift* for 1240 s. During these observations, the X-Ray Telescope (XRT; Burrows et al. 2005) was in photon counting mode (Hill et al. 2004). Source counts were selected in a circular region with a radius of 30 arcsec. Background counts were extracted from a source-free nearby region with a radius of 212 arcsec applying XSELECT. Using the exposure map, an auxiliary response file was created with the tool XRTMKARF. The spectral data were analysed without rebinning in XSPEC (Arnaud 1996) and using Cash statistics (Cash 1979).

The UltraViolet and Optical Telescope (UVOT; Roming et al. 2005) was in event mode with the *UVW2* filter (mode 0x0121). The data for source and background regions were extracted in circles with radii of 7 and 20 arcsec, respectively. Magnitudes and flux densities were determined using UVOTSOURCE with the calibration as described in Poole et al. (2008) and Breeveld et al. (2010).

2.4 Spectroscopy

Phase-resolved spectroscopy with 1 min exposures and a cadence of ≈65.5 s was collected using the Goodman High Throughput Spectrograph on the SOAR telescope (Clemens, Crain & Anderson 2004). A volume-phase holographic (VPH) grating with 930 lines per mm was used, giving a wavelength coverage of approximately 3700–5200 Å. The slit width was 1 arcsec, giving a resolution of 2.9 Å (resolving power ≈1500). These data covered approximately one hour, bracketed by Fe arc lamp exposures before the first spectrum, after half an hour, and after the final spectrum. The spectra were reduced using custom PYTHON-based tools and an optimal extraction routine based on the methods described by Marsh (1989).

A comparison star (*Gaia* EDR3 6058834949186192768, magnitude $G = 16.2$) was also on the slit and observed simultaneously with the target. The comparison star did not have sufficient S/N for analysis within individual exposures. A fit to five Balmer lines in the summed spectrum of the comparison star found that they were consistent with their rest wavelengths (12 ± 16 km s^{-1}).

3 PHOTOMETRIC ANALYSIS

3.1 TESS

In Fig. 1, we show the *TESS* light curve of TIC 378898110. A Lomb-Scargle periodogram (Lomb 1976; Scargle 1982) shows a strong peak with a period of 23.07172(6) min, as well as weaker peaks at harmonics of that signal. The uncertainty on the period was characterized by fitting a sine wave to the data.

When phase-folded on the 23.07 min period (Fig. 1, top right-hand panel), the *TESS* data show non-sinusoidal, sawtooth-like variability, in which the rise is steeper than the decline, which is characteristic of superhump variability in high-state or outbursting AM CVn binaries (e.g. Armstrong, Patterson & Kemp 2012; Green et al. 2018). The bump feature just before minimum light resembles a feature seen in the superhumps of CR Boo early during its outburst (the 'Stage A' superhumps; e.g. Isogai et al. 2016). We also show a phase-fold of the second harmonic of this period, 11.5 min, which gives a somewhat similar form with a weaker amplitude and lower significance.

In order to test for any change in the photometric period, we split the *TESS* light curve into four equal-length segments of approximately 13 days each. Fig. 2 shows the Lomb-Scargle periodograms of the first four harmonics in each of these segments. The period appears constant through the first three segments. However, in the fourth segment, the period appears to drift towards a somewhat lower frequency. The strengths of the higher harmonics change more significantly than the fundamental, but the variation in their

[1] Notable given that the position uncertainty of *ROSAT* sources can be as large as 16 arcsec for low-S/N sources (Ayres 2004).

Downloaded from https://academic.oup.com/mnras/article/527/2/3445/7342474 by guest on 01 December 2023

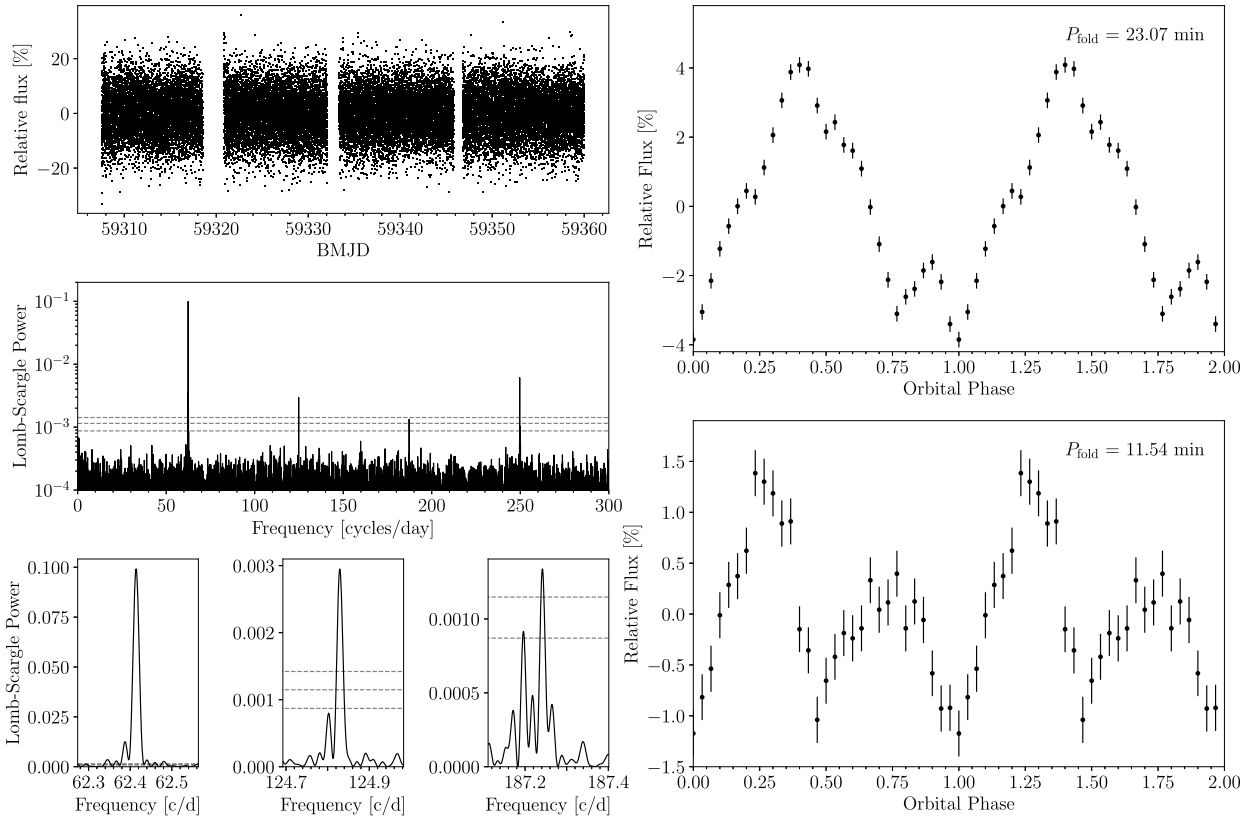

Figure 1. *Top left: TESS* light curve from Sectors 37 and 38, showing flux change relative to the mean. *Middle left:* Lomb-Scargle periodogram of the *TESS* light curve. Dashed horizontal lines show false alarm probabilities of 0.1, 10^{-3}, and 10^{-5}. *Lower left:* Zoomed plots of the periodogram peaks around the 23.07 min period and its first two harmonics, with the same false alarm probabilities marked (c/d refers to cycles per day). Note the change in *y*-axis scale from logarithmic to linear. *Top right:* Phase-folded and binned *TESS* light curve, folded on the 23.07 min period. *Lower right:* Phase-folded and binned *TESS* light curve, folded on the first harmonic at 11.5 min.

frequencies is comparable. After characterising the uncertainties on the fundamental period in each segment by fitting a sine wave to the data, we found that the period drift was significant at a 3-σ level compared to the previous segments. The measured frequencies were 62.415(2), 62.417(2), 62.413(2), and 62.405(2) cycles d^{-1}, respectively, for the four segments.

In the periodogram in Fig. 1, we note a marginal peak with a separation of ≈0.05 per cent at the low-frequency wing of the 23.07 min periodicity and each of its harmonics. This is likely an imprint of the slightly lower frequency seen towards the end of the *TESS* observations.

Unlike in some previously studied systems with space-based photometry (Green et al. 2018; Solanki et al. 2021), we do not see a low-frequency signal resulting from the accretion disc precession in TIC 378898110.

3.2 Ground-based photometry

Figs 3, 4, and 5 show the raw and phase-folded ground-based photometry obtained using SOAR and ULTRACAM, while Figs 6 and 7 show the Lomb-Scargle periodograms. Observations were obtained in 2021 (soon after the *TESS* observations) and in 2022 and 2023. The three sets of observations highlight the changing profile of the variability in TIC 378898110.

The light curves from 2021 show a similar (though not identical) sawtooth-shaped profile as was observed from *TESS*, though with a notably smaller amplitude (≈1 per cent, compared to the ≈4 per cent seen in *TESS*). The high-frequency red noise known as 'flickering' that is typical of accreting systems is also seen. A periodogram of the data from 2021 shows a peak at the 23.07 min period and its second harmonic, with no other significant peaks.

In 2022, the profile of the light curve appeared somewhat different. The middle panel of Fig. 5 shows the phase-folded data from three nights in March 2022. As Fig. 6 shows, the strength of the second harmonic has significantly increased relative to the fundamental frequency of variation. In some 2022 nights, the fundamental frequency is not detected at all, which may be a result of the short observing windows of these observations (60–75 min per night).

Most notably, the precisely measured *TESS* period of 23.07172(6) min did not successfully phase-fold the 2022 ULTRACAM data across multiple nights such that their times of minimum light coincided. Folding the data on the *TESS* period induces a drift of 20 per cent of a phase cycle (≈5 min) between the nights of March 05 and 06. This implies a significant change to the photometric period of at least ≈0.08 min between 2021 and 2022. We found that a folding period of 22.07 min was successful in aligning the light-curve minimima across all three nights in 2022 March, but note that this is only one of a number of equally acceptable aliases.

In 2023, the profile of the light curve was different again. As Fig. 5 shows, the amplitude in 2023 March was ≈4 per cent, similar to that of the *TESS* light curve. The folded light curve shows four peaks per phase cycle, resulting in a strong fourth harmonic of the dominant frequency (Fig. 6). In 2023, as in 2021 but not in 2022, phase-folding the data using the *TESS* period of 23.07172(6) min

Downloaded from https://academic.oup.com/mnras/article/527/2/3445/7342474 by guest on 01 December 2023

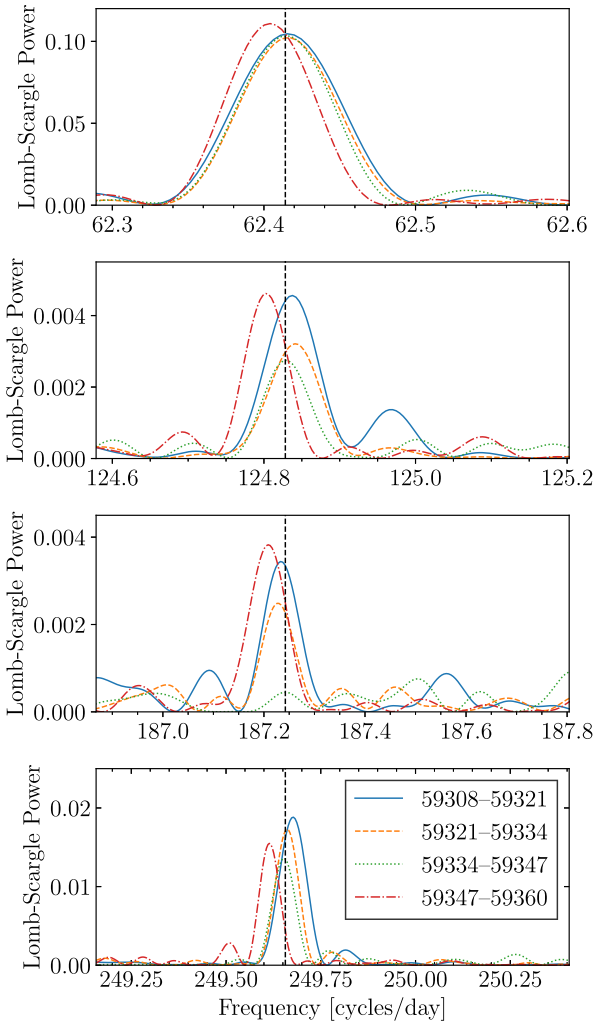

Figure 2. Lomb-Scargle periodograms of *TESS* data, after splitting the data into four equal segments of approximately 13 days each (BJD ranges are denoted in the figure legend). Each row shows one of the four strongest harmonics of the 23.07 min signal. Note that the axis range in each panel has been scaled by the harmonic number, so that a consistent offset in the figure represents a consistent fractional change in frequency between different harmonics. The vertical dashed line shows the 23.07 min signal derived from the combined periodogram of the entire *TESS* light curve and its harmonics. The periodic signal appears to be constant through the first three segments, while it appears to drift towards a slightly lower frequency during the final segment.

successfully aligned the light curve minima across all three nights from 2023 March.

In Fig. 7, we show the combined Lomb-Scargle periodogram of data from two sets of consecutive nights, 2022 March 05–06 and 2023 March 08–10. The strongest alias of the 2023 March data clearly agrees with the *TESS* photometric period. In 2022 March, the favoured values of the periodogram are shifted towards higher frequencies than the *TESS* frequency, and no alias is aligned with the *TESS* frequency. We are therefore confident in claiming that the photometric period observed in 2022 March is different to the period observed in 2021 or 2023. We also note that in 2023, the peaks of the periodograms in g_s and u_s are aligned, while in 2022 they are

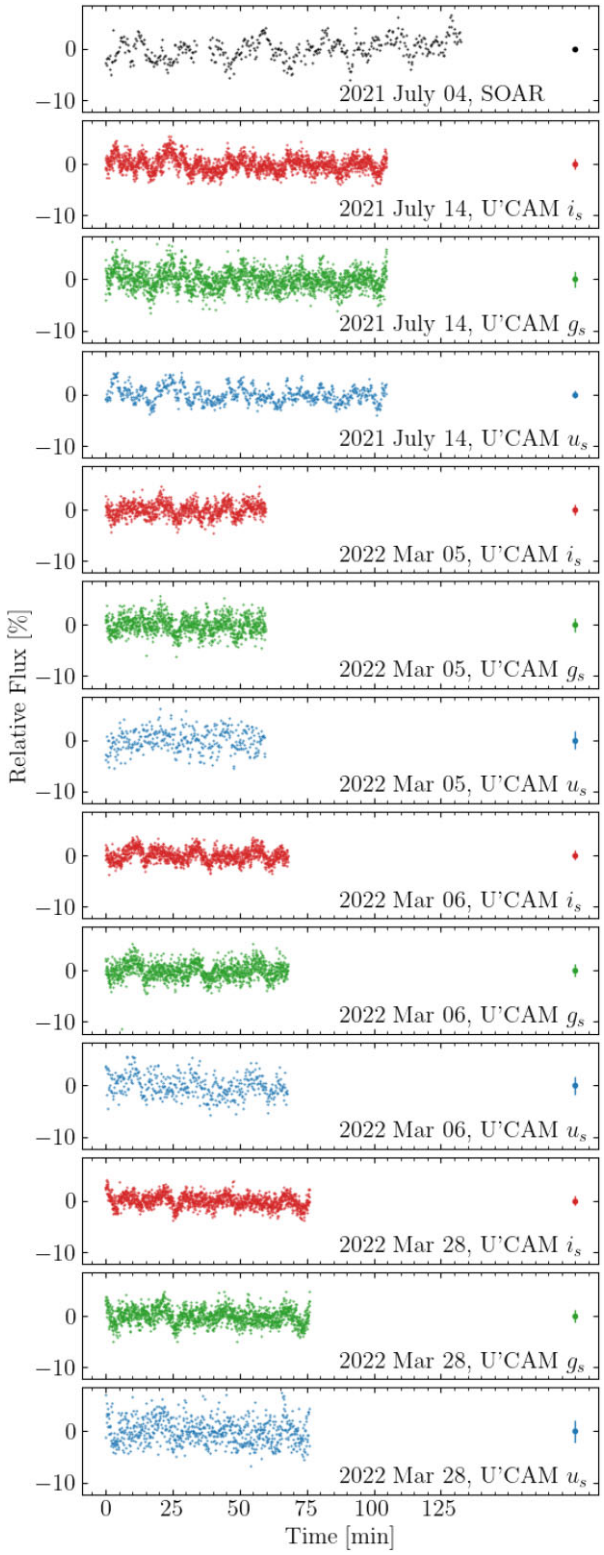

Figure 3. Light curves of TIC 378898110 obtained through an *S8612* filter with Goodman + SOAR and through $u_s g_s i_s$ with ULTRACAM+NTT in 2021 and 2022. Right-hand data point shows the typical uncertainty.

Downloaded from https://academic.oup.com/mnras/article/527/2/3445/7342474 by guest on 01 December 2023

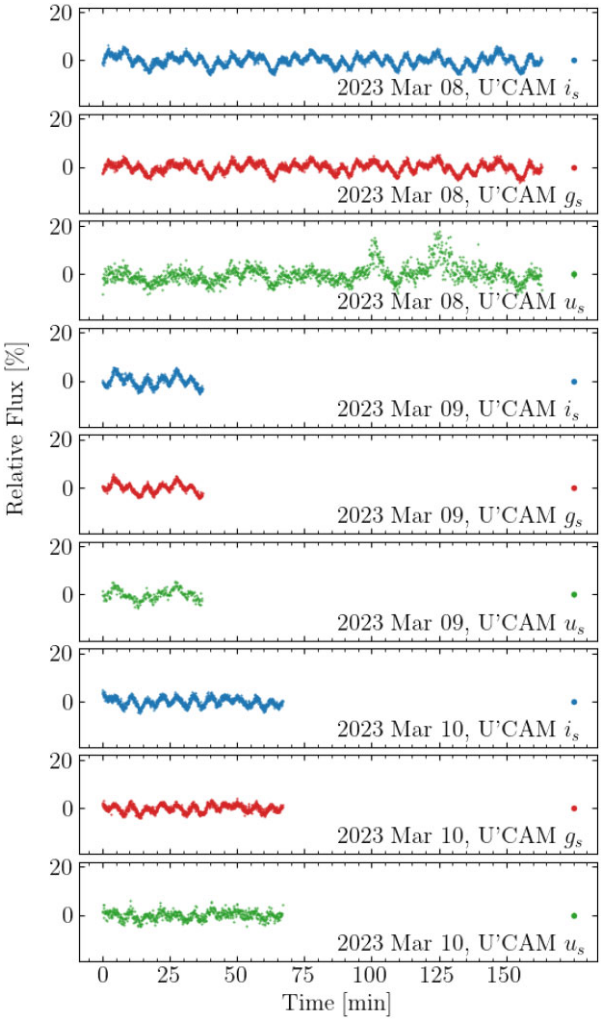

Figure 4. Light curves of TIC 378898110 obtained through $u_s g_s i_s$ filters with ULTRACAM+NTT in 2023.

offset by several aliases relative to each other; this may suggest that the apparent signal seen in 2022 is a combination of two signatures with different characteristic spectra.

Given the complex aliasing (seen in Fig. 7) and the short photometric coverage, it is difficult to precisely quote the 2022 frequency of photometric variability. We estimate by eye that the frequency lies somewhere in the range 70 ± 8 cycles d^{-1}, or 20.5 ± 2.0 min, in the understanding that this is an overestimate of the uncertainty.

3.3 Spectral energy distribution

The Spectral energy distribution (SED) of TIC 378898110 is shown in Fig. 8. In addition to the *Swift* + UVOT data described in Section 2.3, we retrieved data from the *Galaxy Evolution Explorer* (*GALEX*; Morrissey et al. 2007), the American Association of Variable Star Observers (AAVSO) Photometric All-Sky Survey (APASS),[2] *Gaia* Early Data Release 3 (Gaia Collaboration et al. 2021), the Two Micron All Sky Survey (2MASS; Skrutskie et al. 2006), and the Wide-field Infrared Survey Explorer (WISE; Wright et al. 2010).

[2]https://www.aavso.org/apass

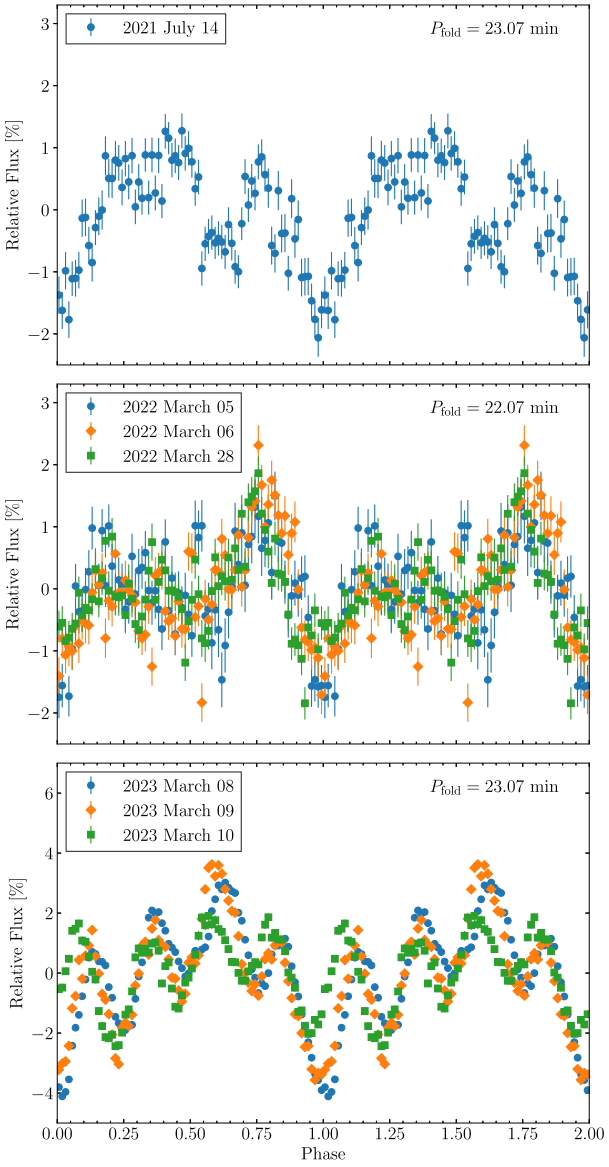

Figure 5. Phase-folded g_s-band ULTRACAM light curve of TIC 378898110 from 2021 (top), 2022 (middle), and 2023 (bottom). Within each panel, data from multiple nights was folded with the same period and phase offset. The zero-phase was chosen as the phase of minimum light. In 2022, folding the data on the *TESS* photometric period of 23.07 min did not reconcile the phase of minimum light between the three nights, and so a different folding period of 22.07 min was used. Note the change in *y*-axis scale between panels. The significant improvement in SNR in 2023 was due to the larger amplitude of the signal and an improvement in atmospheric seeing for the 2023 nights.

There is a factor of two difference in flux between the *Swift* + UVOT *UVW2* measurement (observed 2021 July 27) and the archival GALEX NUV measurement (2011 May 11). The UVOT measurement is easier to reconcile with the optical flux measurements from *Gaia*. As the GALEX NUV measurement is based on only one observation, in which the target is somewhat close to the edge of the detector, we suggest that the measurement is affected by an unknown observational or calibration error. Long-term variability of the source may also contribute to the difference between the UVOT and GALEX fluxes, but it is unlikely to be the entire explanation, because a factor of two change in flux would be unusual for a high-state AM CVn binary. We note that there is

Downloaded from https://academic.oup.com/mnras/article/527/2/3445/7342474 by guest on 01 December 2023

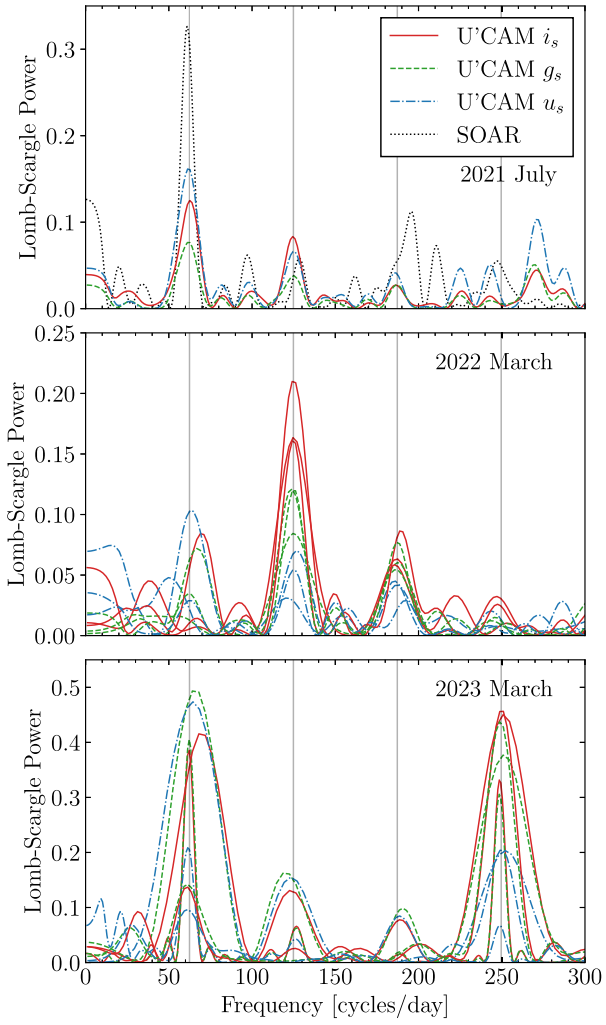

Figure 6. Lomb-Scargle periodograms of the light curves in Figs 3–4, separated into data from 2021, 2022, and 2023. Vertical lines mark the first four harmonics of the *TESS* frequency (23.07 min). The strength of the second harmonic in 2022 and the fourth harmonic in 2023 are significantly increased relative to the fundamental frequency.

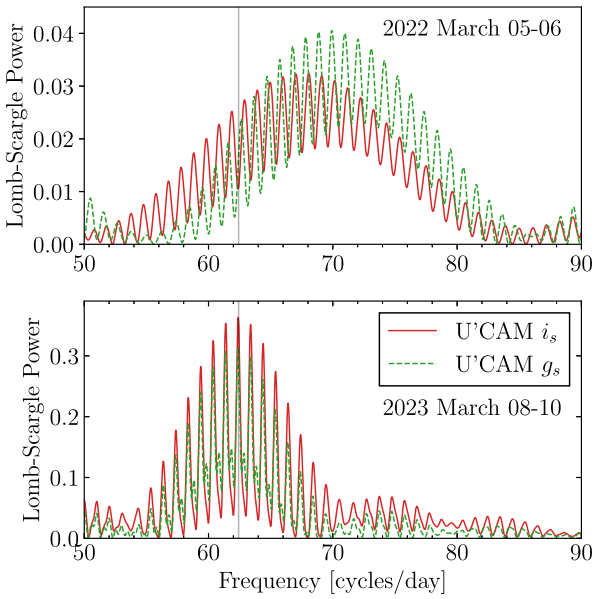

Figure 7. Combined Lomb-Scargle periodograms of multiple nights from 2022 and 2023. The vertical line marks the dominant *TESS* frequency (23.07 min).

also an offset between the optical flux measurements of APASS and *Gaia*, but this smaller difference is easier to explain as resulting from variability of the source. GALEX and APASS data were both excluded from the SED fitting process described below.

The SED cannot be described by a simple blackbody spectrum. This is expected for a high-state AM CVn binary, which is photometrically dominated by the accretion disc.

We modelled the SED of TIC 378898110 using the method applied by Ramsay et al. (2018, their Section 8). It should be emphasized that this method utilizes a number of simplifying assumptions, and provides (at best) an approximation of the true SED. The accretion disc was treated as a set of 200 linearly spaced, concentric, circular[3] annuli, extending from the surface of the accreting white dwarf to an outer disc radius $R_{\rm disc}$. Each annulus was assumed to emit as a blackbody, with the temperature profile of the disc calculated in the standard manner for steady-state accretion discs (e.g. Warner 1995).

The central white dwarf was also treated as a blackbody emitter. The white dwarf radius was calculated from its mass according to a typical carbon-oxygen core mass-radius relationship (Verbunt & Rappaport 1988), and its surface temperature was estimated from the mass transfer rate (Bildsten et al. 2006, their equation 1). Free parameters in the model were the mass transfer rate $\dot{M}$, the primary mass M_1, the outer radius of the disc $R_{\rm disc}$, the orbital inclination i, the distance to the system d, and the interstellar reddening $E(B-V)$.

Gaussian priors were placed on d at 309.3 ± 1.8 pc (according to the *Gaia* parallax measurement) and $E(B-V)$ at 0.11 ± 0.03 (according to the three-dimensional extinction maps of Lallement et al. 2014, 2018; Capitanio et al. 2017).[4] We experimented with applying an additional Gaussian prior on M_1 ($0.8 \pm 0.1\,{\rm M}_\odot$, following typical values for accreting white dwarfs, e.g. Pala et al. 2019), and found that it did not significantly change the other derived parameters. Extinction was calculated using the extinction law of Fitzpatrick (1999) with $R_{\rm V} = 3.1$. The outer disc radius was constrained to the range 0.07–0.11 $R_\odot$, limits which were found by substituting reasonable ranges of primary and secondary masses into two common approximations for the outer disc radius: 30 per cent of the orbital separation and 70 per cent of the primary Roche lobe.

The model was converged on the data by minimizing the χ^2 using a Markov Chain Monte Carlo method (MCMC; Foreman-Mackey et al. 2013) with 32 walkers and 3000 iterations, which was sufficient for the chains to converge. Best-fitting values were determined from the median value of the last 500 iterations, and uncertainties determined as 1.4 × their Median Average Deviation (MAD).

It can be seen in Fig. 8 that the model is somewhat poorly fit to the data. The best-fit model has $\chi^2 = 13.7$ with three degrees of freedom (reduced $\chi^2_{\rm red} = 4.6$). The majority of the fits of Ramsay et al. (2018) have a somewhat better quality, but a minority of their fits are of a comparable quality.[5] The poorer fits, such as this one, are perhaps a

[3]This is a simplification, as in reality the presence of superhump variability implies that the disc is likely to be somewhat eccentric (Patterson, Halpern & Shambrook 1993).

[4]https://stilism.obspm.fr/

[5]We make only a qualitative comparison as no goodness-of-fit parameter was quoted in that work.

Downloaded from https://academic.oup.com/mnras/article/527/2/3445/7342474 by guest on 01 December 2023

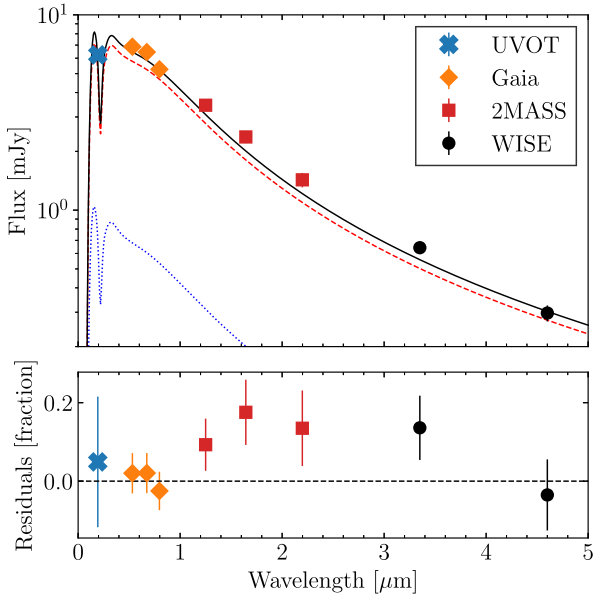

Figure 8. Spectral energy distribution of TIC 378898110. The solid black line shows our best-fit, reddened SED model, which can be decomposed into its accretion disc component (red, dashed) and white dwarf component (blue, dotted). The absorption-like feature at 2175 Å is an imprint of interstellar extinction.

result of the variability of the source between epochs of observation, or perhaps a result of a number of simplifying assumptions made during the modelling process (as detailed above). In particular, the excess in *2MASS* and *WISE* data may result from our overly-simple model of the accretion disc.

The best-fit mass transfer rate was $\log(\dot{M}[\mathrm{M}_\odot\,\mathrm{yr}^{-1}]) = -6.8 \pm 1.0$ when the prior was applied to M_1, or $\log(\dot{M}[\mathrm{M}_\odot\,\mathrm{yr}^{-1}]) = -7.0 \pm 0.8$ otherwise. When compared to other AM CVn binaries that were modelled in a similar way (Ramsay et al. 2018), the estimated mass transfer rate of TIC 378898110 is the second-highest of all systems, beaten only by SDSS J1908+3940. Note that, given the large uncertainties in our mass transfer rate estimate, it is only a 2σ outlier from the general trend found by Ramsay et al. (2018). We also remark that AM CVn itself, perhaps the system most similar to TIC 378898110, was not modelled by Ramsay et al. (2018) due to the large scatter between its flux measurements.

The best-fitting value of M_1 matched the applied prior. When run with no prior on M_1 except an upper limit of 1.4 $\mathrm{M}_\odot$, M_1 was essentially unconstrained. The $E(B-V)$ found was 0.14 ± 0.02, also matching the applied prior. The best-fitting value of i was $74 \pm 10°$, although as with other results quoted in this section, it should be noted that the systematic uncertainties are not fully accounted for.

We experimented with adding a donor star into the SED model. Donor stars are usually not visible in AM CVn binaries, though infrared excesses that may originate from the donor star have recently been observed in several systems (Green et al. 2020; Rivera Sandoval et al. 2021). The donor star was approximated as a blackbody,[6] with its radius fixed to the secondary Roche lobe radius under an assumed donor mass of 0.125 $\mathrm{M}_\odot$ (the same donor mass as AM CVn itself; Roelofs et al. 2006), while the donor temperature was constrained to be less than 8000 K. The addition of a visible donor star slightly decreased the estimated mass transfer rate to $\log(\dot{M}[\mathrm{M}_\odot\,\mathrm{yr}^{-1}]) = 7.0 \pm 0.8$, and did not improve the quality of the fit sufficiently to justify the reduction in the degrees of freedom ($\chi^2 = 10.6$ and reduced $\chi^2_{\mathrm{red}} = 5.3$). We therefore conclude that the donor star is not visible in TIC 378898110.

[6]This simplification was used because reliable spectral models of AM CVn donor stars do not currently exist.

3.4 Mass transfer rate from bolometric magnitude

For comparison with the mass transfer rate derived in the previous section, we tested an alternate method proposed by Roelofs et al. (2007b), in which the system luminosity is assumed to be completely dominated by accretion luminosity. We note that this method systematically returns lower values of $\dot{M}$ than the method of Ramsay et al. (2018); Roelofs et al. (2007b) find values of $\dot{M}$ for HP Lib and GP Com that are factors of ≈3 and ≈10 lower than those of Ramsay et al. (2018).

Following Roelofs et al. (2007b), we used a bolometric correction of -2.5 ± 0.3 (derived in that work under the assumption that the UV flux follows the spectral form of a 30 000 K blackbody) to find the bolometric magnitude from the V-band magnitude. The mass transfer rate can then be derived by assuming that half of the difference in gravitational potential between the inner Lagrange point and the surface of the accretor is released as accretion luminosity. We tested a number of trial values of M_1, M_2, and $\cos i$.

In this manner, mass transfer rates of $\log(\dot{M}[\mathrm{M}_\odot\,\mathrm{yr}^{-1}])$ in the range −8.4 to −9.4 were found (best-fit value of −8.9), with the most critical unknown input being the value of M_1. This value is similar to the values derived by Roelofs et al. (2007b) for the similar short-period system HP Lib. We note that the value derived for AM CVn itself in that work is larger, but this is likely due to the pre-*Gaia* distance estimate being anomalously large (Ramsay et al. 2018).

Due to the systematic uncertainties surrounding the bolometric correction, we favour the results of the SED fitting. That being said, both methods have significant uncertainties and should be interpreted with caution.

3.5 Long-term light curve

In Fig. 9, we show photometry of TIC 378898110 spanning 2000 days from February 2016 to March 2023, retrieved from the All-Sky Automated Search for SuperNovae (ASAS-SN; Shappee et al. 2014; Kochanek et al. 2017). The light curve shows an unusual long-term behaviour, in which the system grew brighter by ≈0.3 mag through 2021, remained bright for much of 2022, and faded again from late 2022 to early 2023.

Given that emission from the system is dominated by the accretion disc, the most likely explanation seems to be a temporary increase in the disc luminosity (due to either an increase in its temperature or radius, or some combination of the two). Using the simple accretion disc model described in Section 3.3, we estimate that a 0.3 mag brightening in g'-band magnitude would necessitate an increase in disc radius of ≈25 per cent or an increase in $\log(\dot{M}/\mathrm{M}_\odot\,\mathrm{yr}^{-1})$ of ≈0.4 dex. For both of these estimates, all other parameters were held constant at their best-fitting values.

Both the amplitude and timescale of the brightening event of TIC 378898110 are somewhat similar to the 'long outburst' phenomena observed in a number of long-period AM CVn binaries (Rivera Sandoval, Maccarone & Pichardo Marcano 2020; Rivera Sandoval et al. 2021; Sunny Wong et al. 2021). Those phenomena have been suggested to result from a temporary increase in $\dot{M}$. However, the nature of TIC 378898110 as a high-state, disc-dominated AM CVn binary is quite different to the long-period, cold-disc AM CVn

Downloaded from https://academic.oup.com/mnras/article/527/2/3445/7342474 by guest on 01 December 2023

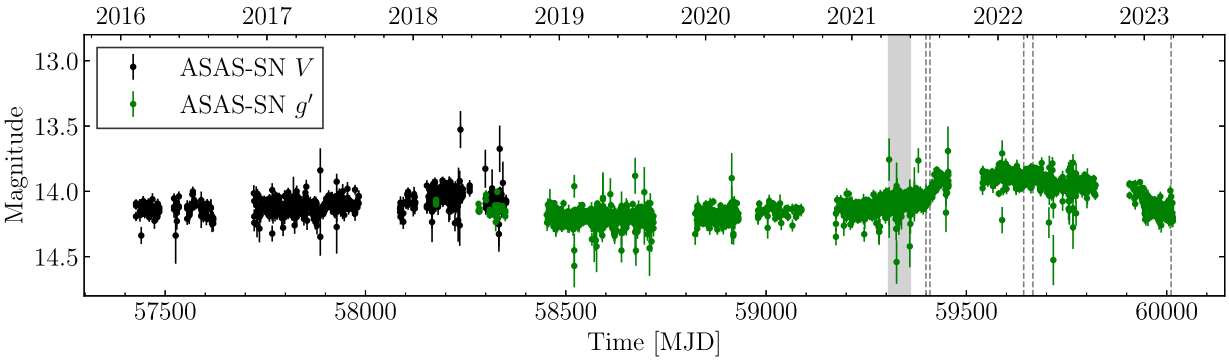

Figure 9. Long-term light curve of TIC 378898110, showing an unusual long-term variation and the absence of outbursts. The observation epoch of *TESS* is shown by the shaded grey region, and those of ULTRACAM by dashed vertical lines.

binaries in which such phenomena have been previously observed. The 'long outburst' phenomena are typically also associated with a reddening of the target, which is not seen here. Comparing the $u_s g_s i_s$ ULTRACAM data, we do not find any measurable colour change between different epochs. Note that this also suggests that a temperature change in the disc is unlikely.

3.6 X-ray detection

X-ray emission in cataclysmic variables and AM CVn binaries originates from the boundary layer between the accretion disc and the accreting white dwarf (Bath et al. 1974), and possibly from a wind emitted by either the disc or the boundary layer (Naylor et al. 1988). X-rays have been detected from a number of AM CVn binary systems across the entire range of orbital periods (van Teeseling & Verbunt 1994; Ramsay et al. 2005, 2006, 2012; Esposito et al. 2014; Wevers et al. 2016; Rivera Sandoval & Maccarone 2019; Rivera Sandoval, Maccarone & Pichardo Marcano 2020; Rivera Sandoval et al. 2021; Maccarone et al. 2023).

Swift + XRT detected 23 photons from TIC 378898110 in 1240 s of observation, leading to a count rate of 0.019 ± 0.004 photons per second. The spectrum was modelled using a power-law distribution. We used an absorption column density of $N_{\rm H} = 0.96 \times 10^{21}$ cm^{-2}, which is calculated from our fitted value $E(B-V) = 0.14$ (Section 3.3) using a conversion factor $N_{\rm H} = 2.21 \times 10^{21} A_{\rm V}$ cm^{-2} (Güver & Özel 2009), with $A_{\rm V} = 3.1E(B-V)$.

The resulting power law had a best-fit index $\Gamma = 2.4 \pm 0.5$. The observed model flux in the range 0.3–10 keV is $9.2^{+4.2}_{-1.8} \times 10^{-13}$ erg cm^{-2} s^{-1}, equivalent to a luminosity of $1.1^{+0.5}_{-0.3} \times 10^{31}$ erg s^{-1} in the same energy range. This value is in the typical range for AM CVn binaries, though with large uncertainties due to the low number of counts (Ramsay et al. 2005, 2006; Rivera Sandoval & Maccarone 2019). We emphasize that the reliability of these results can be improved with further observations.

We performed a search of the 1240 s of *Swift* + UVOT photometry for variability, but given the short observing window that covered less than one orbital cycle, no meaningful upper limit could be derived.

4 SPECTROSCOPIC ANALYSIS

4.1 Average spectrum

The mean spectrum of TIC 378898110 is shown in Fig. 10. It shows a blue continuum and a series of helium absorption lines, as is typical for a high-state AM CVn binary (e.g. Roelofs et al. 2006, 2007a; Fontaine et al. 2011; Kupfer et al. 2015). For comparison, we also show a synthetic, helium-atmosphere (DB) white dwarf spectrum with a temperature[7] of 14 000 K and a surface gravity $\log g = 8.0$ (Cukanovaite et al. 2021). Although similar, the AM CVn spectrum has notable differences, in particular the ratios of relative depths of He I lines. The equivalent widths (EWs) of a selection of He I lines are listed in Table 3.

When compared to the helium lines of AM CVn itself (Roelofs et al. 2006), the helium lines of TIC 378898110 are somewhat narrower and significantly deeper. The helium line profiles of TIC 378898110 each have a single minimum, while the line profiles of AM CVn itself each have two minima, resulting from the blue-shifted and red-shifted limbs of the accretion disc. The narrow, single-core helium lines of TIC 378898110 are more similar to those seen in another high-state AM CVn-type binary, SDSS J1908+3940 (Kupfer et al. 2015). The single-core lines might suggest a relatively face-on inclination, although this would be at odds with the nearly edge-on inclination estimated from our SED fitting (Section 3.3).

Emission from He II is marginally detected (Fig. 11). An absorption feature from Ca II is seen at the K line (the Ca II H line is not detectable due to blending with a nearby He I line). Ca II is also detected in AM CVn itself (e.g. Patterson, Halpern & Shambrook 1993). A shallow absorption feature from 4660–4700 Å may originate from He II or from a combination of He II and Na I, although the presence of Na I would be surprising at the high temperatures implied by the presence of He II. There is an absorption line at approximately 3870 Å, which we could not associate with any element typically seen in AM CVn binaries.

4.2 Searching for periodicity

In Fig. 12, we show trailed spectra of TIC 378898110, generated from the SOAR 1 min spectra and phase-folded on the photometric period of 23.07 min. No periodic pattern is seen in either the trailed spectra (upper panels) or the mean-subtracted trailed spectra (lower panels). We repeated this process for every prominent He I line and still found no evidence for any periodic spectral variability.

As the orbital period is not necessarily the dominant photometric period, we also repeated this process for a further 200 frequencies, equally spaced between 60 and 80 cycles d^{-1}, so as to fully explore the range of possible orbital periods. Folded trailed spectra were

[7]The temperature was chosen by eye to be the best match to the observed spectrum, but this is not in any sense a representation of the true temperature of the AM CVn.

Downloaded from https://academic.oup.com/mnras/article/527/2/3445/7342474 by guest on 01 December 2023

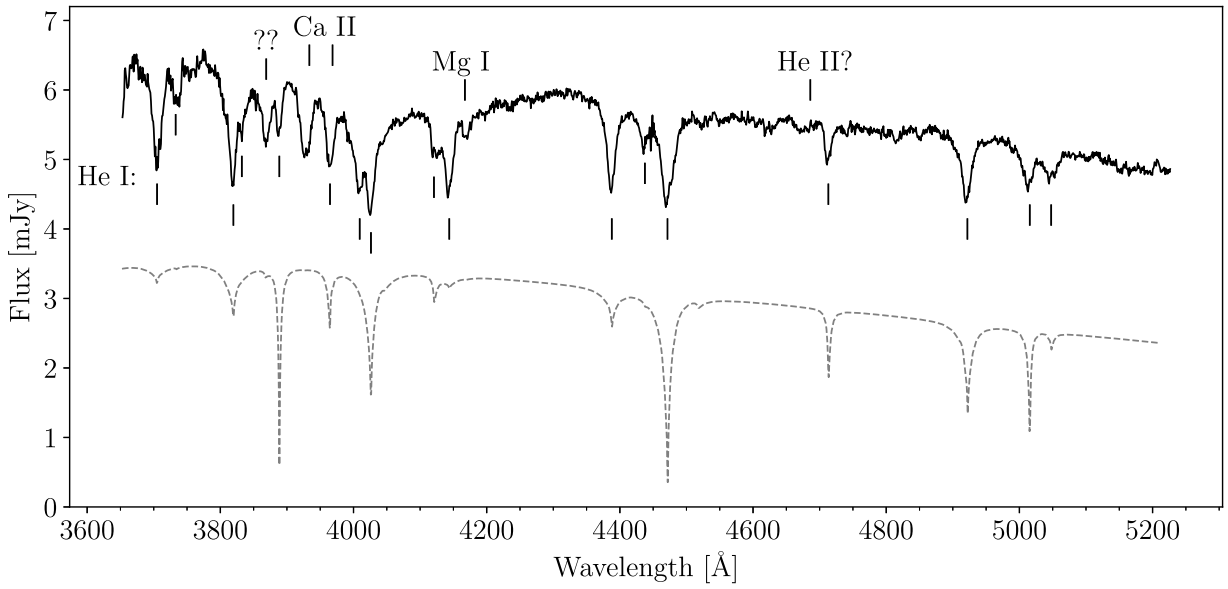

Figure 10. Mean spectrum of TIC 378898110, combining 49 one-minute spectra obtained using Goodman + SOAR on 2021 July 05. Visible features are marked. All tick marks below the spectrum refer to He I. For comparison, we also plot a synthetic, 14 000 K, $\log g = 8.0$, helium-atmosphere white dwarf spectrum (grey, dashed) from Cukanovaite et al. (2021) scaled to the same mean flux and offset by −3.5 mJy.

Table 3. Equivalent widths of selected He I lines in the mean spectrum of TIC 378898110.

Wavelength [Å]	EW [Å]
3888.6	0.53 ± 0.07
4120.8	0.29 ± 0.06
4387.9	3.57 ± 0.05
4471.5	4.02 ± 0.05
4713.1	1.79 ± 0.06
4921.9	3.02 ± 0.06
5015.7	1.93 ± 0.06

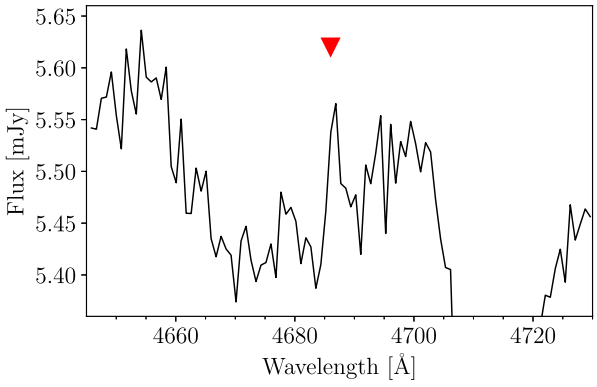

Figure 11. Zoomed mean spectrum of TIC 378898110 around the He II 4686 Å line. The expected wavelength of the line is shown with the red triangle. An emission line is marginally detected.

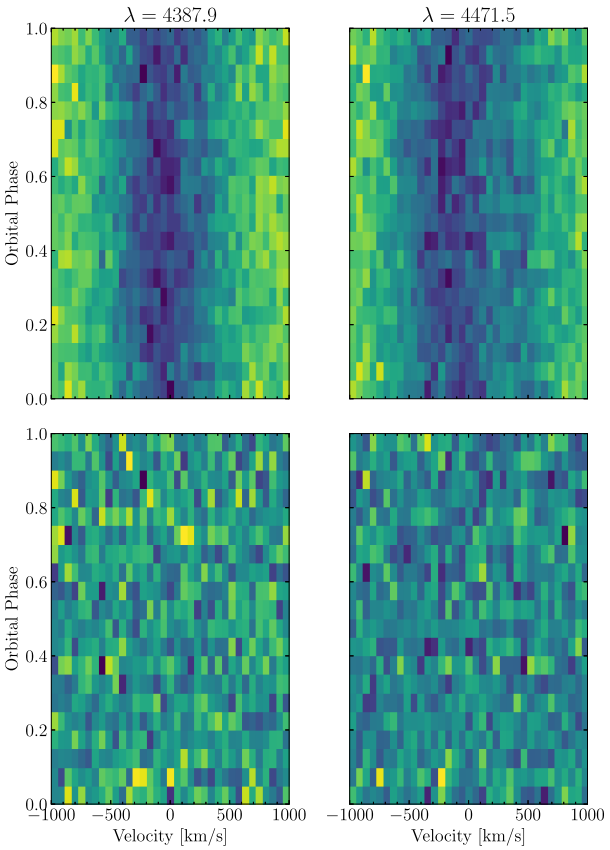

Figure 12. *Top row:* Trailed spectra of TIC 378898110 from 2021 July 05, created using 49 back-to-back, one-minute exposures with Goodman + SOAR, phase-folded on the 23.07 min period and showing the 4387.9 and 4471.5 Å He I lines (left and right, respectively). *Bottom row:* The same trailed spectra with the mean spectrum (Fig. 10) subtracted from each. We do not see any periodic feature in the residuals.

produced using each candidate period, for four spectral lines: He I 4387.9 Å, He I 4471.5 Å, Mg I 4167.3 Å, and Ca I 3933.7 Å. No periodic signal was visible at any of the tested periods in any of the investigated lines.

Most AM CVn binaries show spectral emission from a bright spot feature, located at the intersection between the infalling accretion stream and the edge of the accretion disc, the radial velocity of

Downloaded from https://academic.oup.com/mnras/article/527/2/3445/7342474 by guest on 01 December 2023

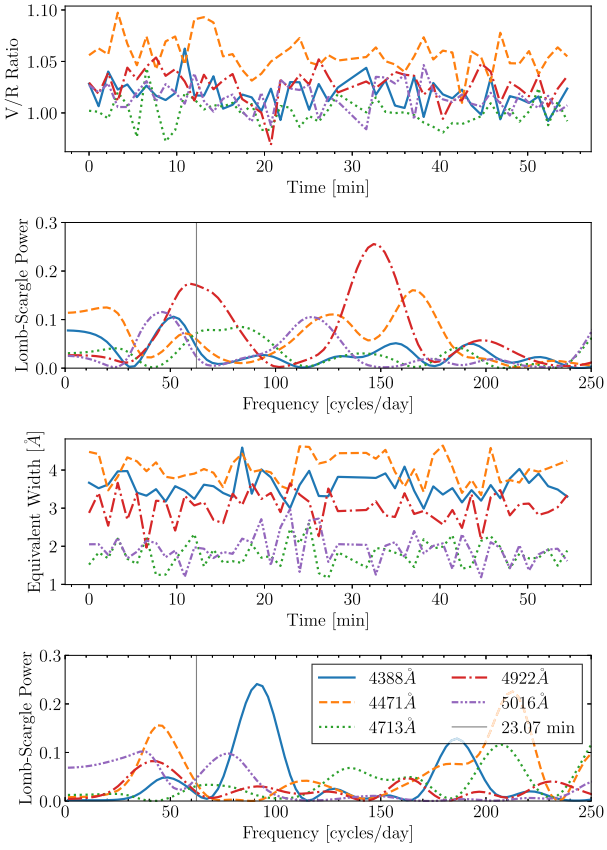

Figure 13. Measured V/R ratios and equivalent widths of five He I lines from the one-minute Goodman + SOAR spectra, and Lomb-Scargle periodograms of those measurements. On the periodograms, the 23.07-min photometric period is marked with a dashed vertical line. In no line do we detect variability commensurate with the photometric periods.

which varies as a function of orbital phase (e.g. Kupfer et al. 2015). The absence of such a feature in TIC 378898110 is notable. Such features are not usually difficult to detect in low-state systems, but can be much harder to detect in high-state systems, often requiring high-resolution observations (e.g. Roelofs et al. 2006). The system with the most similar spectrum, SDSS J1908+3940, shows periodic variability in only some of its absorption lines (Kupfer et al. 2015).

We further searched for periodic patterns in two properties of the helium line profiles of TIC 378898110: the violet-to-red ratio (V/R) and equivalent width (EW) of each line. The V/R ratio of a spectral line is the ratio of the integral under the violet wing of the line ($\lambda < \lambda_c$, where λ_c is the central wavelength of the line as tabulated in Table 3) to the integral under the red wing of the line ($\lambda > \lambda_c$). For each of the 1 min exposure time SOAR spectra, both V/R ratio and EW were measured from each of the five strongest helium absorption lines. In Fig. 13, we plot both properties over time, as well as a Lomb-Scargle periodogram of each. There is no periodicity that is significantly detected (the most prominent peak, for the V/R ratio of the 4922 Å line, has a false alarm probability of nine per cent).

In addition, we searched for periodic variations in the shape of the spectral lines using the USURPER algorithm (Unit-Sphere Representation PERiodogram), a form of phase-distance correlation periodogram (Zucker 2018; Binnenfeld, Shahaf & Zucker 2020).[8]

[8]Implemented using the SPARTA package (SPectroscopic vARiabiliTy Analysis) of Shahaf et al. (2020).

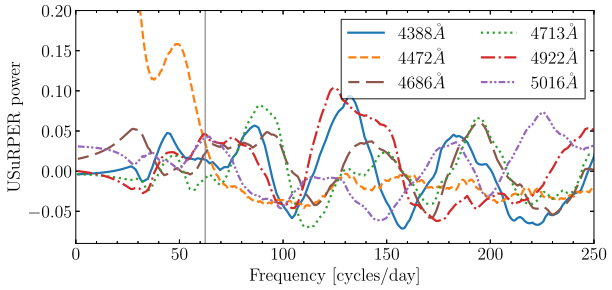

Figure 14. Phase-distance correlation periodograms of five He I lines and the He II line at 4686 Å from the one-minute Goodman + SOAR spectra, calculated using the USURPER algorithm.

The USURPER algorithm searches for periodic changes in the overall shape of a set of input spectra, with no model-dependent assumptions about the underlying line shapes. Once again we found no significant periodicity (Fig. 14).

5 DISCUSSION

5.1 The nature of the photometric periods

In previously studied AM CVn binaries in high state or during outburst, the dominant photometric period is usually the superhump period (e.g. Roelofs et al. 2006; Armstrong, Patterson & Kemp 2012; Isogai et al. 2019; Pichardo Marcano et al. 2021), although exceptions exist (Kupfer et al. 2015). When the orbital and superhump periods are both visible, it can be difficult to disentangle them without extended, continuous coverage (Green et al. 2018). As 23.07172(6) min is the only detected signal in the *TESS* coverage of TIC 378898110, the most natural interpretation is that this is the superhump period. Assuming a typical superhump excess of 1–3 per cent would imply an orbital period in the range of 22–23 min.

The period appears constant through most of the *TESS* data. Towards the end of the coverage, a small-scale period change of order $\Delta P/P \sim 10^{-4}$ was detected. Changes on a similar scale were detected in some of the periodic signals in SDSS J1908+3940 (Kupfer et al. 2015), but not in the orbital signature. The higher harmonics of the signatures in TIC 378898110 show changes in amplitude (Fig. 2), which were also seen in some periodic signals in SDSS J1908+3940, though Kupfer et al. (2015) do not comment on the harmonics of the orbital signature in particular.

In 2022, TIC 378898110 underwent two changes in its observed properties. First, the system brightened by 0.3 mag for the majority of 2022, before returning to its original brightness (Fig. 9). As discussed in Section 3.5, the change in brightness may be driven by a change in disc radius or temperature (the latter being closely linked to the mass transfer rate). Secondly, the dominant photometric period changed from the period seen in *TESS*, 23.07172(6) min, in July 2021 to a shorter period (20.5 ± 2.0 min) in March 2022, before returning to a period consistent with the *TESS* period by the time of our March 2023 observations (Fig. 7). While the quoted uncertainties (limited by nightly aliases) are formally consistent between the two periods, the fact that no alias is consistent with the *TESS* period suggests that there was at least some change in the period in 2022. The closest alias to the *TESS* period differs by 0.4 cycles d^{-1} ($\Delta P/P \approx 0.006$). The July 2021 observations were during the system's rise in brightness (Fig. 9), while the March 2022 were during the brightness plateau, and March 2023 was following the descent back to its quiescent

Downloaded from https://academic.oup.com/mnras/article/527/2/3445/7342474 by guest on 01 December 2023

magnitude. It seems natural to suggest there is a link between the two observed changes.

A change to the superhump period of this scale is not expected for a disc that is stably high or quiescent. However, photometric period changes of a similar scale can be seen when a system is rising into outburst compared to the peak of the outburst ('Stage A' compared to 'Stage B' superhumps. e.g. Kato et al. 2009; Kato & Osaki 2013; Isogai et al. 2016). Those period changes are suggested to arise due to a change in the precession rate of the disc, which may, for instance, be driven by a change in which regions of the disc drive the overall precession rate (Osaki & Kato 2013). It may be that a similar change in disc state, related to the proposed increase in disc radius or mass transfer rate, might explain the difference in period between the 2022 data set and the 2021 and 2023 data sets.

Alternatively, if the disc did indeed grow in radius during 2022, it may have entered a radius range in which the edge of the disc can be eclipsed by the donor star. The phase-folded light curve from 2022 (Fig. 5) is somewhat similar in profile and amplitude to the disc-eclipsing binary PTF J1919+4815 (Levitan et al. 2014). The inclination of PTF J1919+4815, 76–79°, is consistent with the inclination of TIC 378898110 that we estimate from our SED fitting ($74 \pm 10°$, Section 3.3). Under this interpretation, the 20.5 ± 2.0 min photometric period seen in 2022 would be the orbital period, or perhaps a blend of the unresolved superhump and orbital periods, as was seen by Green et al. (2018). The fact that periodograms of g_s and i_s data from March 2022 peak at different frequencies (Fig. 7), unlike those from March 2023, which are consistent between filters, also suggests a contribution from two unresolved periodic signals with different spectral profiles.

We consider the latter to be a more likely interpretation. An orbital period in this range would be consistent with the 23.07 min superhump period. However, it is not possible to confirm this interpretation on the basis of the data that are currently available. Further follow-up observations such as sustained, high-resolution spectroscopy, or photometry during a future brightening episode, may finally confirm the orbital period of this system.

5.2 Gravitational wave radiation

Given its (probable) short orbital period and close distance, the gravitational wave emission of TIC 378898110 is likely to be strong. Using the package LEGWORK (Wagg, Breivik & de Mink 2022a, b), we estimate the signal-noise ratio (SNR) that can be achieved for TIC 378898110 using *LISA*. We adopted the estimated distance of 306.2 ± 1.7 pc, orbital period of 20.5 ± 1.5 min, orbital inclination of $74 \pm 10°$, primary mass $0.8 \pm 0.1\,M_\odot$, and secondary mass $0.125 \pm 0.04\,M_\odot$. The latter is based on the secondary mass of AM CVn itself (Roelofs et al. 2006), with error bars large enough to include other typical values for AM CVn binaries at this orbital period (e.g. Green et al. 2018; van Roestel et al. 2022).

The expected SNR is $2.8^{+1.5}_{-0.9}$, $4.9^{+2.4}_{-1.6}$, 24^{+15}_{-9}, and 73^{+52}_{-25}, after 1, 2, 4, and 10 yr of *LISA* observations. The dominant uncertainties come from the secondary mass, the orbital period, and the inclination. Further observations may be able to more precisely measure these properties, and make TIC 378898110 a valuable verification target for *LISA* (Kupfer et al. 2018, 2023).

6 SUMMARY AND CONCLUSIONS

TIC 378898110 is a bright system that shows photometric modulation on a period of 23.07 min, first discovered in 2-min-cadence *TESS* observations. Its spectrum, photometric period, and accretion-driven photometric flickering support its classification as a high-state AM CVn binary system. The 23.07 min period is most likely to be the superhump period; if so, then the orbital period is likely to be in the range of 22–23 min. This makes TIC 378898110 the shortest period binary system discovered by *TESS* so far. It is the third-brightest AM CVn binary system known, but has avoided detection until now, likely due to the absence of the photometric outbursts by which AM CVn binaries are often discovered.

During 2021–2022, the system underwent an unusual brightening event with an amplitude of 0.3 mag, which lasted for approximately one year. At the same time, the dominant photometric period appears to have changed from 23.07 min to a shorter period in the range 18.5–22.5 min. We propose an interpretation of these two changes in which an increase in the accretion disc radius (driven by an unknown cause) made the system brighter and caused the onset of disc-edge eclipses. By early 2023, both the system brightness and the photometric period had returned to their previously recorded values.

Using an SED fit, we estimate that the mass transfer rate of the binary is unusually large ($\log(\dot{M}[M_\odot\,\mathrm{yr}^{-1}]) = -6.8 \pm 1.0$) when compared to other AM CVn binaries modelled in the same way. This may help to explain how the system is able to sustain a high-state accretion disc at an implied orbital period of 22–23 min. A high mass-transfer rate may be driven by a donor star which is unusually high-mass or thermally inflated.

Given the nearby distance (306.2 pc) and short orbital period (22–23 min), TIC 378898110 is likely to be a detectable source of gravitational waves with planned space-based detectors. We estimate that *LISA* is likely to be able to make a 3σ detection of TIC 378898110 in its first two years of operation. Further electromagnetic observations of TIC 378898110 to fully characterize the system will make it a valuable verification binary system for *LISA* (Kupfer et al. 2018, 2023).

It is remarkable that high-state AM CVn binary systems have now been serendipitously discovered in each of *Kepler*, *K2*, and *TESS* (Fontaine et al. 2011; Green et al. 2018, and this work). Because high-state AM CVn systems do not undergo photometric outbursts, they are most easily found by short-cadence, high-precision photometric surveys. The discovery of TIC 378898110 reinforces the suggestion, implied by the distance distribution of AM CVn binaries (Ramsay et al. 2018), that a number of AM CVn binaries remain hidden even among bright and nearby stars. Searches for blue, short-period variables in large photometric surveys (see also Burdge et al. 2020a; van Roestel et al. 2022) are valuable tools to find these hidden AM CVn binaries.

ACKNOWLEDGEMENTS

We are grateful to the anonymous reviewer for feedback which has significantly improved the quality of the manuscript. MJG was supported by the European Research Council (ERC) under the European Union's FP7 Programme, Grant No. 833031 (PI: Dan Maoz). JJH acknowledges support through TESS Guest Investigator Program 80NSSC22K0737. This project has received funding from the European Research Council (ERC) under the European Union's Horizon 2020 research and innovation programme (Grant agreement No. 101020057). BNB acknowledges support through TESS Guest Investigator Programs 80NSSC19K1720 and 80NSSC21K0364. TRM and IP were supported by the UK's Science and Technology Facilities Council (STFC), grant ST/T000406/1. IP additionally acknowledges a Warwick Astrophysics prize post-doctoral fellowship made possible thanks to a generous philanthropic donation. VSD and ULTRACAM are funded by the UK's Science

Downloaded from https://academic.oup.com/mnras/article/527/2/3445/7342474 by guest on 01 December 2023

and Technology Facilities Council (STFC), grant ST/V000853/1. ASB was supported by the National Science Centre under project No. UMO-2017/26/E/ST9/00703. SGP acknowledges the support of a STFC Ernest Rutherford Fellowship. ADR and SOK were supported by Conselho Nacional de Desenvolvimento Científico e Tecnológico - Brasil (CNPq). This research was supported in part by the National Science Foundation under Grant No. NSF PHY-1748958 (Kavli Institute of Theoretical Physics).

This work made use of the software IRAF, XSPEC, and DAOPHOT, as well as the PYTHON packages NUMPY, MATPLOTLIB, SCIPY, ASTROPY, EMCEE and EXTINCTION.

This paper includes data collected by the *TESS* mission. Funding for the *TESS* mission is provided by the National Aeronautics and Space Administration (NASA)'s Science Mission Directorate. This research is based in part on observations obtained at the Southern Astrophysical Research (SOAR) telescope, which is a joint project of the Ministério da Ciência, Tecnologia, e Inovação (MCTI) da República Federativa do Brasil, the U.S. National Optical Astronomy Observatory (NOAO), the University of North Carolina at Chapel Hill (UNC), and Michigan State University (MSU). This work is based in part on observations collected at the European Organisation for Astronomical Research in the Southern Hemisphere under ESO programmes 105.D-0761, 0108.D-0718, and 0110.D-4325. This research made use of the AAVSO Photometric All-Sky Survey (APASS), funded by the Robert Martin Ayers Sciences Fund and NSF AST-1412587.

DATA AVAILABILITY

The 2-min *TESS* data used in this work are publicly available via the Barbara A. Mikulski Archive for Space Telescopes (MAST). SED data displayed in Fig. 8 are also publicly available. Other data will be made available on reasonable request to the authors.

REFERENCES

Armstrong E., Patterson J., Kemp J., 2012, MNRAS, 421, 2310
Arnaud K. A., 1996, in Jacoby G. H., Barnes J., eds, ASP Conf. Ser. Vol. 101, Astronomical Data Analysis Software and Systems V. Astron. Soc. Pac., San Francisco, p. 17
Ayres T. R., 2004, ApJ, 608, 957
Bailer-Jones C. A. L., Rybizki J., Fouesneau M., Demleitner M., Andrae R., 2021, AJ, 161, 147
Bath G. T., Evans W. D., Papaloizou J., Pringle J. E., 1974, MNRAS, 169, 447
Belloni D., Schreiber M. R., 2023, A&A, 678, A34
Bildsten L., Townsley D. M., Deloye C. J., Nelemans G., 2006, ApJ, 640, 466
Bildsten L., Shen K. J., Weinberg N. N., Nelemans G., 2007, ApJ, 662, L95
Binnenfeld A., Shahaf S., Zucker S., 2020, A&A, 642, A146
Breeveld A. A. et al., 2010, MNRAS, 406, 1687
Breivik K., Kremer K., Bueno M., Larson S. L., Coughlin S., Kalogera V., 2018, ApJ, 854, 1
Burdge K. B. et al., 2020a, ApJ, 905, 32
Burdge K. B. et al., 2020b, ApJ, 905, L7
Burrows D. N. et al., 2005, Space Sci. Rev., 120, 165
Cannizzo J. K., Nelemans G., 2015, ApJ, 803, 19
Capitanio L., Lallement R., Vergely J. L., Elyajouri M., Monreal-Ibero A., 2017, A&A, 606, A65
Carter P. J. et al., 2013, MNRAS, 429, 2143
Cash W., 1979, ApJ, 228, 939
Clemens J. C., Crain J. A., Anderson R., 2004, Proc. SPIE, 5492, 331
Cukanovaite E., Tremblay P.-E., Bergeron P., Freytag B., Ludwig H.-G., Steffen M., 2021, MNRAS, 501, 5274
Deloye C. J., Taam R. E., Winisdoerffer C., Chabrier G., 2007, MNRAS, 381, 525
Dhillon V. S. et al., 2007, MNRAS, 378, 825
Dhillon V. S. et al., 2021, MNRAS, 507, 350
Esposito P., Israel G. L., Dall'Osso S., Covino S., 2014, A&A, 561, A117
Fitzpatrick E. L., 1999, PASP, 111, 63
Fontaine G. et al., 2011, ApJ, 726, 92
Foreman-Mackey D., Hogg D. W., Lang D., Goodman J., 2013, PASP, 125, 306
Gaia Collaboration et al., 2021, A&A, 649, A1
Gehrels N. et al., 2004, ApJ, 611, 1005
Geier S., Raddi R., Gentile Fusillo N. P., Marsh T. R., 2019, A&A, 621, A38
Goliasch J., Nelson L., 2015, ApJ, 809, 80
Green M. J. et al., 2018, MNRAS, 477, 5646
Green M. J. et al., 2020, MNRAS, 496, 1243
Güver T., Özel F., 2009, MNRAS, 400, 2050
Higgins M. E., Bell K. J., 2023, AJ, 165, 141
Hill J. E. et al., 2004, in Flanagan K. A., Siegmund O. H. W., eds, SPIE conf. Ser. Vol. 5165, X-Ray and Gamma-Ray Instrumentation for Astronomy XIII. SPIE,Bellingham, WA, USA, p. 217
Iben I. J., Tutukov A. V., 1987, ApJ, 313, 727
Isogai K. et al., 2016, PASJ, 68, 64
Isogai K., Kato T., Monard B., Hambsch F.-J., Myers G., Starr P., Cook L. M., Nogami D., 2019, Publ. Astron. Soc. Japan, 71, 48
Kato T., Osaki Y., 2013, PASJ, 65, 115
Kato T. et al., 2009, PASJ, 61, S395
Kilic M. et al., 2014, MNRAS, 438, L26
Kochanek C. S. et al., 2017, PASP, 129, 104502
Kremer K., Breivik K., Larson S. L., Kalogera V., 2017, ApJ, 846, 95
Kupfer T. et al., 2015, MNRAS, 453, 483
Kupfer T. et al., 2018, MNRAS, 480, 302
Kupfer T. et al., 2023, preprint (arXiv:2302.12719)
Lallement R., Vergely J. L., Valette B., Puspitarini L., Eyer L., Casagrande L., 2014, A&A, 561, A91
Lallement R. et al., 2018, A&A, 616, A132
Levitan D. et al., 2014, ApJ, 785, 114
Lomb N. R., 1976, Astrophys. Space Sci., 39, 447
Maccarone T. J., Kupfer T., Najera Casarrubias E., Rivera Sandoval L., Shaw A., Britt C., van Roestel J., Zurek D., 2023, preprint (arXiv:2302.12318)
Maoz D., Mannucci F., Nelemans G., 2014, ARA&A, 52, 107
Marsh T. R., 1989, PASP, 101, 1032
Morrissey P. et al., 2007, ApJS, 173, 682
Naylor T., Bath G. T., Charles P. A., Hassall B. J. M., Sonneborn G., van der Woerd H., van Paradijs J., 1988, MNRAS, 231, 237
Osaki Y., Kato T., 2013, PASJ, 65, 50
Paczyński B., 1967, Acta Astronomica, 17, 287
Pala A. F. et al., 2019, MNRAS, 494, 3799
Patterson J., Halpern J., Shambrook A., 1993, ApJ, 419, 803
Pichardo Marcano M., Rivera Sandoval L. E., Maccarone T. J., Scaringi S., 2021, MNRAS, 508, 3275
Podsiadlowski P., Han Z., Rappaport S., 2003, MNRAS, 340, 1214
Poole T. S. et al., 2008, MNRAS, 383, 627
Ramsay G., Hakala P., Wu K., Cropper M., Mason K. O., Córdova F. A., Priedhorsky W., 2005, MNRAS, 357, 49
Ramsay G., Groot P. J., Marsh T., Nelemans G., Steeghs D., Hakala P., 2006, A&A, 457, 623
Ramsay G., Wheatley P. J., Rosen S., Barclay T., Steeghs D., 2012, MNRAS, 425, 1486
Ramsay G. et al., 2018, A&A, 620, A141
Ricker G. R. et al., 2014, Proc. SPIE, 9143, 914320
Rivera Sandoval L. E., Maccarone T. J., 2019, MNRAS, 483, L6
Rivera Sandoval L. E., Maccarone T. J., Pichardo Marcano M., 2020, ApJ, 900, L37
Rivera Sandoval L. E., Maccarone T. J., Cavecchi Y., Britt C., Zurek D., 2021, MNRAS, 505, 215
Roelofs G. H. A., Groot P. J., Nelemans G., Marsh T. R., Steeghs D., 2006, MNRAS, 371, 1231

Downloaded from https://academic.oup.com/mnras/article/527/2/3445/7342474 by guest on 01 December 2023

Roelofs G. H. A., Groot P. J., Nelemans G., Marsh T. R., Steeghs D., 2007a, MNRAS, 379, 176
Roelofs G. H. A., Groot P. J., Benedict G. F., McArthur B. E., Steeghs D., Morales-Rueda L., Marsh T. R., Nelemans G., 2007b, ApJ, 666, 1174
Roming P. W. A. et al., 2005, Space Sci. Rev., 120, 95
Savonije G. J., de Kool M., van den Heuvel E. P. J., 1986, A&A, 155, 51
Scargle J. D., 1982, ApJ, 263, 835
Shahaf S., Binnenfeld A., Mazeh T., Zucker S., 2020, SPARTA: SPectroscopic vARiabiliTy Analysis, Astrophysics Source Code Library. record(ascl:2007.022)
Shappee B. J. et al., 2014, ApJ, 788, 48
Skrutskie M. F. et al., 2006, AJ, 131, 1163
Solanki S., Kupfer T., Blaes O., Breedt E., Scaringi S., 2021, MNRAS, 500, 1222
Solheim J.-E., 2010, PASP, 122, 1133
Sunny Wong T. L., van Roestel J., Kupfer T., Bildsten L., 2021, Res. Notes AAS, 5, 3
Tsugawa M., Osaki Y., 1997, PASJ, 49, 75
van Roestel J. et al., 2021, AJ, 162, 113
van Roestel J. et al., 2022, MNRAS, 512, 5440
van Teeseling A., Verbunt F., 1994, A&A, 292, 519
Verbunt F., Rappaport S., 1988, ApJ, 332, 193
Wagg T., Breivik K., de Mink S., 2022a, J. Open Source Softw., 7, 3998
Wagg T., Breivik K., de Mink S. E., 2022b, ApJS, 260, 52
Warner B., 1995, Cataclysmic Variable Stars. Cambridge Univ. Press, Cambridge
Wevers T. et al., 2016, MNRAS, 462, L106
Wong T. L. S., Bildsten L., 2021, ApJ, 923, 125
Wright E. L. et al., 2010, AJ, 140, 1868
Yungelson L. R., 2008, Astron. Lett., 34, 620
Zucker S., 2018, MNRAS, 474, L86

[1]*Max-Planck-Institut für Astronomie, Königstuhl 17, D-69117 Heidelberg, Germany*
[2]*School of Physics and Astronomy, Tel-Aviv University, Tel-Aviv 6997801, Israel*
[3]*Astronomy and Astrophysics Group, Department of Physics, University of Warwick, Coventry, CV4 7AL, United Kingdom*
[4]*Department of Astronomy, Boston University, 725 Commonwealth Ave., Boston, MA 02215, USA*
[5]*Department of Physics and Astronomy, High Point University, High Point, NC 27268, USA*
[6]*Department of Physics and Astronomy, University of North Carolina, Chapel Hill, NC 27599, USA*
[7]*Instituto de Física, Universidade Federal do Rio Grande do Sul, Av. Bento Goncalves 9500, Porto Alegre 91501-970, RS, Brazil*
[8]*Instituto de Física y Astronomía, Universidad de Valparaíso, Gran Bretaña 1111, Playa Ancha, Valparaíso 2360102, Chile*
[9]*University of Virginia, Department of Astronomy, 530 McCormick Rd., Charlottesville, VA 22904, USA*
[10]*Department of Physics, Geology, and Engineering Technology, Northern Kentucky University, Highland Heights, KY 41076, USA*
[11]*School of Physics, University College Cork, Cork, T12 K8AF, Ireland*
[12]*Jodrell Bank Centre for Astrophysics, Department of Physics and Astronomy, The University of Manchester, Manchester M13 9PL, UK*
[13]*Isaac Newton Group of Telescopes, Apartado de Correos 368, E-38700 Santa Cruz de La Palma, Spain*
[14]*ARDASTELLA Research Collaboration, Missouri State University, Springfield, MO 65897, USA*
[15]*Astronomical Observatory, University of Warsaw, Al. Ujazdowskie 4, PL-00-478 Warszawa, Poland*
[16]*Institute of Astronomy, University of Cambridge, Madingley Road, Cambridge, CB3 0HA, United Kingdom*
[17]*Department of Physics and Astronomy, University of Sheffield, Sheffield, S3 7RH, United Kingdom*
[18]*Instituto de Astrofísica de Canarias, E-38205 La Laguna, Tenerife, Spain*
[19]*Department of Astronomy, University of Michigan, Ann Arbor, MI 48109, USA*

This paper has been typeset from a TEX/LATEX file prepared by the author.

Downloaded from https://academic.oup.com/mnras/article/527/2/3445/7342474 by guest on 01 December 2023

© The Author(s) 2023.
Published by Oxford University Press on behalf of Royal Astronomical Society. This is an Open Access article distributed under the terms of the Creative Commons Attribution License (http://creativecommons.org/licenses/by/4.0/), which permits unrestricted reuse, distribution, and reproduction in any medium, provided the original work is properly cited.